



## Ceria–gadolinia supported NiCu catalyst: A suitable system for dry reforming of biogas to feed a solid oxide fuel cell (SOFC)

G. Bonura\*, C. Cannilla, F. Frusteri

CNR-ITAE "Nicola Giordano" Via S. Lucia Sopra Contesse, 5 – 98126 Messina, Italy

### ARTICLE INFO

#### Article history:

Received 22 December 2011

Received in revised form 19 March 2012

Accepted 27 March 2012

Available online 3 April 2012

#### Keywords:

Biogas conversion

Dry reforming

Solid oxide fuel cells

NiCu alloy

### ABSTRACT

NiCu/Ce<sub>0.9</sub>Gd<sub>0.1</sub>O<sub>2-δ</sub> (CGO) catalysts were prepared by different techniques with the aim to develop a bifunctional catalyst, characterized both by catalytic and anodic properties for integrated biogas SOFC process. Catalytic measurements have been performed in CO<sub>2</sub> reforming of CH<sub>4</sub>, using a fixed bed reactor at a reaction temperature ranging from 650 to 800 °C. Results revealed that NiCu/CGO system is a promising catalyst for the conversion of biogas mixtures at temperature suitable to be used in low temperature solid oxide fuel cell (LT-SOFC). Characterization data clearly demonstrated that NiCu alloy forms by reduction of NiCuO<sub>x</sub> mixed oxide patches, while catalytic testing showed carbon-free operation at 800 °C (GHSV = 6600 h<sup>-1</sup>) when "CO<sub>2</sub>-rich" biogas mixtures are used. By a thermodynamic evaluation of the different reaction kinetics, the poor efficiency of the catalyst in promoting the carbon gasification by CO<sub>2</sub> reaction has been assessed. Characterization of spent catalysts shed light both on the reasons of deactivation phenomena occurring with time over the catalysts and on the deactivation kinetics under the adopted experimental conditions.

© 2012 Elsevier B.V. All rights reserved.

### 1. Introduction

Solid oxide fuel cell (SOFC) technology attracts much interest thanks to the flexibility that it offers to be fed, besides pure hydrogen, with other fuels. In this respect, biogas mainly consisting of CO<sub>2</sub> and CH<sub>4</sub> can be considered an attractive renewable carbon source obtainable by fermentation of organic compounds (sewage sludges, liquid organic industrial effluents, farms residues, landfill, municipal and industrial solid organic residues) [1] and its exploitation would be advantageous from both economical and environmental point of view. In fact, it could represent a valid alternative to pure methane being indigenous, free of non-methane hydrocarbons, and containing a large fraction of CO<sub>2</sub> that is a methane-reforming agent.

Recently, a 100 kW SOFC system fed by biogas mixtures has been proposed, with an electrical efficiency of almost 48.7% [2], compared to 41.5% of a conventional system [3]. Its performance was still remarkable even at low methane content in biogas, since a drop of only 5% was observed when CH<sub>4</sub> concentration was reduced from 70 to 30 mol% [4]. Indeed, the development of fuel cells directly fed with biogas at different composition is of great practical importance. In this fuel cell "concept", the methane

dry-reforming reaction could occur internally, without the necessity of an external reformer to produce H<sub>2</sub> to feed the anode.

Currently, industrial catalysts used to produce hydrogen by reforming processes are not suitable for dry reforming reaction, mainly due to the difficulty to manage the coke formation occurring during reaction. Basically, among the possible strategies to avoid or limit the amount of coke formed, the choice of a suitable carrier or the utilization of active phase(s) alternative to the mostly conventional metals, is the approach normally followed. On this account, in the last years, several efforts have been devoted to develop catalysts characterized by high efficiency and lifetime in dry reforming conditions and, in particular, Ni [5–13] and supported noble metals catalysts [14–21] have been widely investigated. Noble metals based catalysts show more resistance towards coke formation than Ni catalysts [18–21], but for large use they are too expensive. For this reason, the research strategy is focused on the individuation of "low cost" catalytic formulations.

In view of the development of a suitable material for the internal reforming in a SOFC (SOFC-IR), it is necessary to consider the composition of the conventional anodic cermet too. On this account, while yttrium-stabilized zirconia (YSZ) is often used in high temperature SOFCs, ceria-based materials show significantly higher ionic conductivity and enhanced direct oxidation of hydrocarbons due to the rapid lattice oxygen mobility [22,23]. Indeed, under reduction atmosphere, ceria doped with rare earths, i.e. gadolinia, is a good mixed electronic-ionic conductor not considerably affected by coke deposition at anode [22,23]. Unfortunately,

\* Corresponding author. Tel.: +39 090 624 294; fax: +39 090 624 247.

E-mail address: [giuseppe.bonura@ita.cnr.it](mailto:giuseppe.bonura@ita.cnr.it) (G. Bonura).

the catalytic activity of ceria at temperature lower than 800 °C, that is the temperature at which a low temperature solid oxide fuel cell (LT-SOFC) works, is low in dry reforming conditions, so the use of an active phase is necessary. Therefore, the coupling of Ni with ceria–gadolinia should allow to improve the catalytic activity of the system, enhancing the oxidation rate of hydrogen and providing electronic conductivity for the anode, although the formation of coke due to the presence of Ni could limit SOFC lifetime [22,23].

In this respect, it has been already envisaged that, during reforming reaction catalyzed by Ni, the type and the amount of carbon species formed depend both on reaction conditions and on metal particle size or metal–support interaction [24,25]. In particular, carbon deposition should be favoured when Ni metal particles size is greater than 5–10 nm [24,25]. Ni particles could be decreased promoting the formation of solid solutions [26] or by sulphiding Ni catalysts [27]. Also the addition of Cu to Ni based catalyst can modify the Ni ensemble environment by forming a NiCu alloy [23,24,28]. Unlike Ni, Cu is a poor catalyst for carbon growth, but effective as current collector. With NiCu alloys based anodes for IT-SOFC, carbon deposition can be substantially suppressed and the electrochemical activity of cell can be maintained for long time [23]. Besides, NiCu alloys have been already successfully investigated as anodes in molten carbonate fuel cells [29] or as catalysts for steam reforming [30,31] or ethylene hydrogenation processes [32].

On the basis of the above considerations, in this paper the attention was devoted to prepare different NiCu based catalysts at high metal loading (*ca.* 70 wt%) by using gadolinia-doped ceria (CGO) as oxide carrier [22], with the aim to design an efficient system suitable to be used as catalyst and anode in a SOFC fed by biogas. Different preparation methods have been employed for the NiCu alloys formation, in order to confer higher resistance towards coke formation during internal reforming of methane, especially as the operating temperature of SOFCs is decreased.

## 2. Experimental

### 2.1. Catalysts preparation

CGO ( $\text{Ce}_{0.9}\text{Gd}_{0.1}\text{O}_{2-\delta}$ ) powder, with a chemical purity of 99.9%, an average particle size ( $d_{50}$ ) of 0.50  $\mu\text{m}$  and a surface area of 7.8  $\text{m}^2 \text{ g}^{-1}$ , was synthesized *via* combustion spray pyrolysis method by Praxair Inc. (Specialty Ceramics).

*Impregnation.* N5C4-W1 catalyst was prepared by wet impregnation method, using an aqueous solution of  $\text{Ni}(\text{NO}_3)_2 \cdot 6\text{H}_2\text{O}$  and  $\text{Cu}(\text{NO}_3)_2 \cdot 2.5\text{H}_2\text{O}$  precursors and CGO as carrier, in a weight ratio NiCu:CGO = 7:3. A catalyst containing *ca.* 75 wt% of Ni and Cu loading was obtained. At the end of the impregnation, the catalyst was dried at 110 °C and calcined at 500 °C for 3 h.

*Coprecipitation.* N5C4-P1 catalyst was prepared using an aqueous solution of  $\text{Ni}(\text{NO}_3)_2 \cdot 6\text{H}_2\text{O}$  and  $\text{Cu}(\text{NO}_3)_2 \cdot 2.5\text{H}_2\text{O}$  as precursors (Cu/Ni atomic ratio of 0.8), directly added dropwise to a 0.1 M  $\text{NaHCO}_3$  solution, containing a defined amount of dispersed CGO (for a final catalyst containing 30 wt% of CGO), in an ultrasonic bath at 44 kHz. During the coprecipitation, the slurry was stirred vigorously at 60 °C and the pH was kept at 7.0–7.5 by the continuous addition of a 0.1 M  $\text{NaHCO}_3$  solution. Then, the solid was held under ultrasound irradiation for 1 h at 60 °C, repeatedly washed and filtered. The solid so obtained was dried at 110 °C and calcined at 500 °C for 3 h.

*Coprecipitation and mechanical mixing.* N5C4-P2 was prepared by coprecipitation method, slowly adding  $\text{Cu}(\text{NO}_3)_2 \cdot 2.5\text{H}_2\text{O}$  and  $\text{Ni}(\text{NO}_3)_2 \cdot 6\text{H}_2\text{O}$  (Cu/Ni atomic ratio of 0.8) to a  $\text{NaHCO}_3$  solution at pH = 7, under ultrasound irradiation at 44 kHz. Also in this case, during the coprecipitation, the slurry was stirred vigorously at 60 °C and the pH was kept at 7.0–7.5 by the continuous addition of a

0.1 M  $\text{NaHCO}_3$  solution. After that, the solid was washed in distilled water, filtered and dried at 110 °C. Calcination was carried out at a temperature of 500 °C for 3 h. Then, the  $\text{NiCuO}_x$  phase was mechanically mixed in an agate mortar with CGO in a weight ratio NiCu:CGO = 7:3.

*Combustion and mechanical mixing.* N5C4-F2 catalyst was prepared using an aqueous solution of  $\text{Cu}(\text{NO}_3)_2 \cdot 2.5\text{H}_2\text{O}$  and  $\text{Ni}(\text{NO}_3)_2 \cdot 6\text{H}_2\text{O}$  that was concentrated in a hot-plate at 300 °C. A known amount of oxalic dihydrazide (ODH) was gradually added for the reduction of the nitrate precursors. At last, the cup was quickly put in an oven preheated at 420 °C to complete the combustion. After the firing step, a sponge-like shaped catalyst was obtained. In order to remove carbon residues formed during the combustion, catalyst was further calcined at 500 °C for 1 h. Such a sample was mechanically mixed in an agate mortar with CGO in a weight ratio of 7:3.

*Commercial NiO mixed with CGO (N9C0).* As a reference, a copper-free catalyst was prepared by mixing in an agate mortar a commercial NiO powder (99%, Aldrich) with CGO in a weight ratio of 7:3.

### 2.2. Catalysts characterization

*Surface area and pore volume (PV).* SA and PV values of catalysts were determined from nitrogen adsorption–desorption isotherms at –196 °C, using a Sorptomatic 1900 (Carlo Erba Instrument) gas adsorption device. The isotherms were elaborated according to the BET method for SA calculation, while Horwarth–Kavazoe (HK) and Barrett–Joyner–Halenda (BJH) methods were used for micro and mesopores evaluation, respectively.

*X-ray fluorescence (XRF).* Metal loading was determined by X-ray fluorescence analysis, using a BRUKER AXS – S4 Explorer spectrometer, equipped with a Rhodium X-ray source (Rh anode and 75  $\mu\text{m}$  Be-window). Samples were analyzed at the solid state calculating the emission value of  $\text{Ni}-\text{K}_{\alpha 1}$  and  $\text{Cu}-\text{K}_{\alpha 1}$  transitions. The analytical composition of catalysts was expressed in atomic percentage both of  $\text{Ni}^0$  and  $\text{Cu}^0$ .

*X-ray diffraction (XRD).* Analysis of powdered catalysts was carried out using a Philips X-Pert diffractometer operating with monochromatic  $\text{CuK}_{\alpha}$  ( $\lambda = 1.54056 \text{ \AA}$ ) at 40 kV and 20 mA. Scans were registered in the  $2\theta$  range of 10–90°, with a scan speed of 0.05°/s or 0.0133°/s, in order to determine the crystallographic parameters, the composition of the NiCu alloy as well as the relative concentration of different metal phases. The assignment of the diffraction peaks and the identification of crystalline phases were carried out by comparing the data obtained with the compounds in the JCPDS database. The lattice spacing “ $a$ ” of the NiCu alloy has been calculated considering the integral intensities of the (200) lines by the formula:

$$a_{200} = \lambda_{\text{K}\alpha 1} \sin \theta_{\max}^{-1} \quad (1)$$

where “ $\lambda$ ” is the wavelength of the Cu X-ray source and “ $\theta_{\max}$ ” is the Bragg angle. The fraction of Cu ( $\chi_{\text{Cu}}$ ) in the NiCu alloy was determined by using the Vegard's law according to the follow empirical relationship:

$$\chi_{\text{Cu}} = \frac{a_{200} - a_{\text{Ni}}}{a_{\text{Cu}} - a_{\text{Ni}}} \quad (2)$$

where “ $a_{\text{Ni}}$ ” (3.5238  $\text{\AA}$ ) and “ $a_{\text{Cu}}$ ” (3.6150  $\text{\AA}$ ) are the lattice dimensions of the fcc structures of Ni and Cu respectively. Changes in the particle size (before and after the use) were estimated by using Sherrer's equation.

*Temperature programmed reduction (TPR).* The measurements were performed in a linear quartz micro-reactor (i.d. 4 mm) fed with a 5 vol.%  $\text{H}_2/\text{Ar}$  purified carrier at the flow rate of 30 STP ml  $\text{min}^{-1}$ . The experiments were carried out in the range

**Table 1**  
Physico-chemical properties of the prepared systems.

Catalyst	Preparation method	Analytical composition			Textural properties		
		$\chi_{\text{Ni}}$ (atm/atm)	$\chi_{\text{Cu}}$ (atm/atm)	Ni + Cu (wt%)	$S_{\text{BET}}$ ( $\text{m}^2 \text{g}^{-1}$ )	PV ( $\text{cm}^3 \text{g}^{-1}$ )	APP ( $\text{\AA}$ )
N9CO	Mechanical mixing of commercial NiO with CGO	1.00	0.00	68.3	3.7	0.04	396
N5C4-W1	Wet impregnation of metal precursors over CGO	0.58	0.42	74.5	15.9	0.05	128
N5C4-P1	Coprecipitation of metal precursors in a solution of dissolved CGO	0.55	0.45	71.7	117.5	0.11	37
N5C4-P2	Coprecipitation of metal precursors and mixing with CGO	0.56	0.44	67.1	119.1	0.13	44
N5C4-F2	Combustion of metal precursors and mixing with CGO	0.57	0.43	64.4	5.3	0.03	226

100–800 °C with a heating rate of 10 °C min<sup>-1</sup>. The hydrogen consumption was monitored by a TCD, calibrated by the peak area of known amounts of CuO. TPR data resulted very reproducible both in maximum position ( $\pm 3$  °C) and extent of H<sub>2</sub> consumption ( $\pm 3\%$ ).

**Thermogravimetry (TG).** Spent catalysts were studied by TG analysis for determining the amount of coke formed during reaction. The combustion of carbonaceous deposits was monitored by heating 15–20 mg of sample in a thermo-balance Netzsch STA 409 from 20 to 920 °C ( $\beta = 5$  °C min<sup>-1</sup>) in static air atmosphere.

**Transmission electron microscopy (TEM).** In order to get information on morphological nature of coke formed, TEM analysis of “used” catalyst was performed by a Philips CM12 microscope (resolution, 0.2 nm). Powdered samples were dispersed in *i*-propyllic alcohol under ultrasound irradiation and the resulting suspensions were put dropwise on a standard copper grid coated with a porous carbon film.

### 2.3. Catalytic testing

Experiments were carried out using a stainless steel plug-flow reactor (i.d. 10 mm) by operating at atmospheric pressure and reaction temperature ranging from 650 to 800 °C. A CO<sub>2</sub>/CH<sub>4</sub> reaction mixture, simulating a biogas composition, was fed at the rate of 55 STP mL min<sup>-1</sup> on a 0.05–0.5 g catalyst sample diluted with 0.5 g of same-sized SiC (40–70 mesh). N<sub>2</sub> was used as internal standard for on-line GC analysis. Prior to each test, the catalyst was reduced *in situ* at 825 °C for 1 h flowing 100 mL min<sup>-1</sup> of hydrogen at atmospheric pressure. Catalytic data were also obtained by changing the CO<sub>2</sub>/CH<sub>4</sub> ratio between 0.5 and 2, in order to explore the optimal experimental conditions for reducing coke formation rate. The reaction stream was analyzed on-line by a GC equipped with a two-column system connected to FID for CH<sub>4</sub> analysis and TCD for H<sub>2</sub>, CO<sub>2</sub>, N<sub>2</sub>, CO analysis, respectively.

## 3. Results

### 3.1. Catalyst characterization

The chemical composition along with the textural properties of the prepared catalysts is reported in Table 1. As it is possible to notice, all the catalysts are characterized by an almost constant Cu/Ni atomic ratio (~0.8), while the weight percentage of metallic phase (Ni + Cu) ranges from 64.4 to 74.5%. The complete removal of Na<sup>+</sup> ions in the coprecipitated catalysts was confirmed by XRF. Moreover, independently of the method used to “combine” nickel and copper precursors with CGO, either directly into the precipitating solution (N5C4-P1 sample) or after mechanical mixing with the calcined NiCuO<sub>x</sub> phase (N5C4-P2 sample), the coprecipitation under ultrasound allows to form solid systems with a large surface exposure, resulting 117.5 m<sup>2</sup> g<sup>-1</sup> for N5C4-P1

and 119.1 m<sup>2</sup> g<sup>-1</sup> for N5C4-P2 samples, respectively. On the contrary, the combustion method promotes the formation of dense structures characterized by low surface area (5.3 m<sup>2</sup> g<sup>-1</sup>) as a consequence of shrinkage porosity occurring during firing at high temperature. Yet, the impregnation of CGO with the metal precursors (N5C4-W1 sample) results in an increase of the total surface area (from 7.8 to 15.9 m<sup>2</sup> g<sup>-1</sup>), evidently due to the contribution of the supported oxides.

In order to evaluate how preparation method affects the structural properties of the prepared catalysts, in Fig. 1 the XRD profiles of the calcined systems are depicted along with diffraction pattern of bare CGO. As it is possible to observe, only in the samples prepared by combustion (N5C4-F2) and impregnation (N5C4-W1) methods, the typical diffraction peaks of NiO are well visible. In particular, N5C4-F2 sample exhibits CuO and NiO crystallized in monoclinic (JCPDS 05-0661) and trigonal (JCPDS 22-1189) structures respectively, without any evident interaction among the different oxides. However, by comparing XRD spectra of N5C4-F2 catalyst before and after mixing with CGO (see the inset in Fig. 1), change in the size of nickel particles is observable, with smaller particles (15–20%) in presence of CGO, reflecting the occurrence of a strong metal support interaction (SMSI) [33]. XRD pattern of N5C4-W1, instead, reveals the presence of NiO with a *fcc* cubic structure (JCPDS 04-0835). The subsequent refinement of XRD data, by using a pseudo-Voigt model, showed that the slightly asymmetric peak at 37° could also hide the formation of a mixed oxide Cu<sub>x</sub>Ni<sub>1-x</sub>O (JCPDS 25-1049) that would indicate an incipient formation of solid

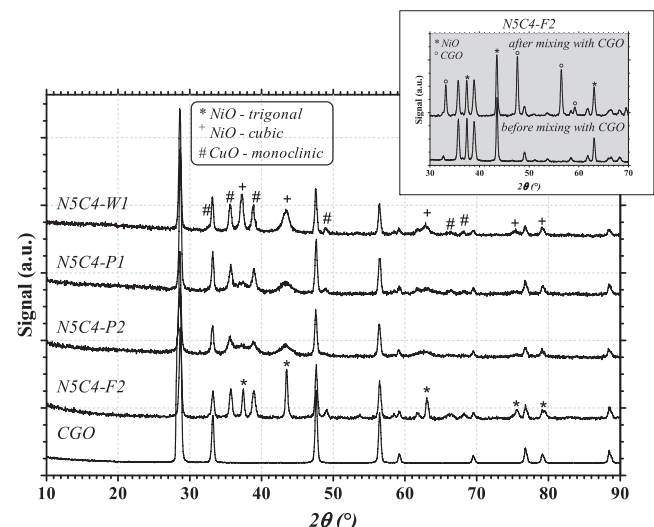


**Fig. 1.** Diffraction pattern of CGO-supported NiCu catalysts calcined at 500 °C. In the inset, XRD patterns of N5C4-F2 before and after mixing with CGO.

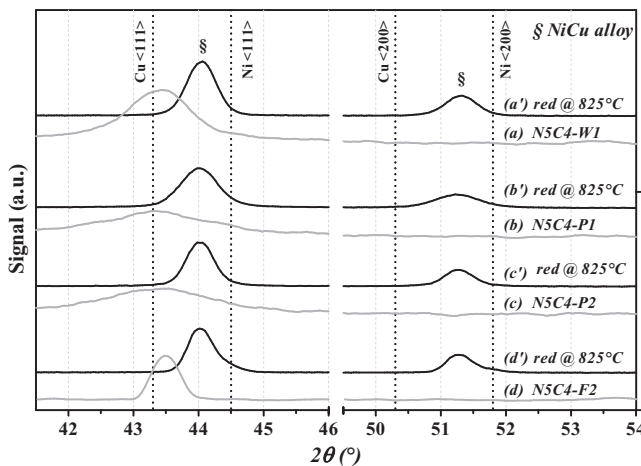


Fig. 2. Comparison of XRD patterns of calcined and reduced catalysts:  $2\theta$  range 42–54°. Dotted lines refer to metallic Cu and Ni signals.

solution in cubic phase, as confirmed by Furtado et al. [30]. On the contrary, by comparing the diffractograms of the coprecipitated systems, N5C4-P1 and N5C4-P2, the NiO peak at 37° appears less intense, being partially “choked” between the two neighbouring CuO peaks. Indeed, Ni oxide species are likely present in such samples in amorphous or microcrystalline phase(s) with highly dispersed crystallites [34], which account for a more intimate contact among the oxide phases, owing to the coprecipitation method that hinders the growth of isolated crystalline domains.

Nevertheless, since on the basis of literature evidences [23,28,35] it is also possible to form a NiCu alloy by reduction of calcined catalysts in which the presence of “ideal” NiO–CuO solid solutions cannot be ascertained, X-ray diffraction measurements were performed on catalysts reduced at 825 °C. In Fig. 2 the diffraction patterns of the calcined and reduced samples are compared in the enlarged 42–54°  $2\theta$  range. As a reference, the diffraction lines of pure Cu<sup>0</sup> (JCPDS 04-0836) and Ni<sup>0</sup> (JCPDS 04-0850) are also shown. Noticeably, on all the investigated catalysts, irrespectively from the preparation method, the peaks correspondent to “single” metals are not detectable, but only a single metallic phase is observed, ascribable to the formation of a NiCu alloy upon reduction of the NiCuO<sub>x</sub> system [36]. Indeed, the diffraction peaks of the alloy are at around 43.9, 51.2 and 75.3°, in intermediate position to those attributable to metallic Ni and Cu lines, anyway at lower angles than pure Ni<sup>0</sup>, consistently with the fact that the atomic radius of Cu ( $r = 128$  pm) is bigger than that of Ni ( $r = 124$  pm) [23,37]. No other Ni or Cu species were detected in the XRD patterns of the reduced samples. Really, since the mixing enthalpy of copper and nickel is small and positive [38] and both metals have a fcc structure, a NiCu alloy, maintaining the cubic structure, can be easily formed not only in the narrow range of composition investigated ( $\chi_{\text{Cu}}$  0.42–0.45), but also over the entire atomic composition range [39].

As a further indication of the formation of NiCu alloys after H<sub>2</sub> reduction, in Table 2 the lattice constants “ $a$ ” of the reduced samples were reported, as calculated from the diffraction peak corresponding to the reflection (200) of the NiCu alloy (51.2°) in a cubic packing. These values well match with the theoretical values expected from Vegard's law [5], monotonically varying with the Cu atomic fraction ( $\chi_{\text{Cu}}$ ) in the alloy. In fact, the largest lattice spacing (3.566 Å) is related to the catalyst (N5C4-P1) with the largest copper atomic fraction (0.463), whereas N5C4-W1 with the smallest copper atomic fraction (0.422) exhibits the lowest lattice constant value calculated (3.562 Å). Consistently with this result, the diffraction peak of the alloy observed at around 44°, in case of N5C4-W1,

Table 2  
Crystallographic parameters of the reduced NiCu catalysts.

Catalyst	$2\theta$ (°)	$a_{200}$ (Å)	$\chi_{\text{Cu}}^{\text{a}}$
		Reduced	
N9C0	51.86	–	0.000
N5C4-W1	51.27	3.562	0.422
N5C4-P1	51.21	3.566	0.463
N5C4-P2	51.24	3.564	0.444
N5C4-F2	51.27	3.562	0.423

<sup>a</sup> Copper atomic fraction in the NiCu alloy.

was slightly shifted to higher angle due the highest amount of pure Ni<sup>0</sup> present.

In Fig. 3 the reduction profiles of the prepared catalysts are shown, while the correspondent quantitative data, in terms of onset reduction temperature ( $T_{0,\text{red}}$ ), maximum reduction temperature ( $T_{Mn}$ ) and hydrogen consumption, are reported in Table 3. TPR profiles of pure CuO, NiO and CuO–NiO mechanical mixture are also presented for comparison. As it is possible to observe, CGO results almost not reducible in H<sub>2</sub> atmosphere in the temperature range considered, showing a modest hydrogen consumption (1.1 mmol H<sub>2</sub>/g<sub>cat</sub>) only at temperature higher than 600 °C.

Differently, all the TPR patterns of the NiCu/CGO samples are significantly affected by the preparation method, with two main reduction maxima shifted in the ranges 200–252 °C ( $T_{M0}$ ) and 262–316 °C ( $T_{M1}$ ), well below than those found for the pure oxides CuO or NiO, which exhibit reduction maxima at 280 and 383 °C respectively. In particular, the coprecipitated N5C4-P1 and N5C4-P2 samples display TPR profiles characterized by similar reduction kinetics, with two evident peaks at 200–212 °C and 262–266 °C,

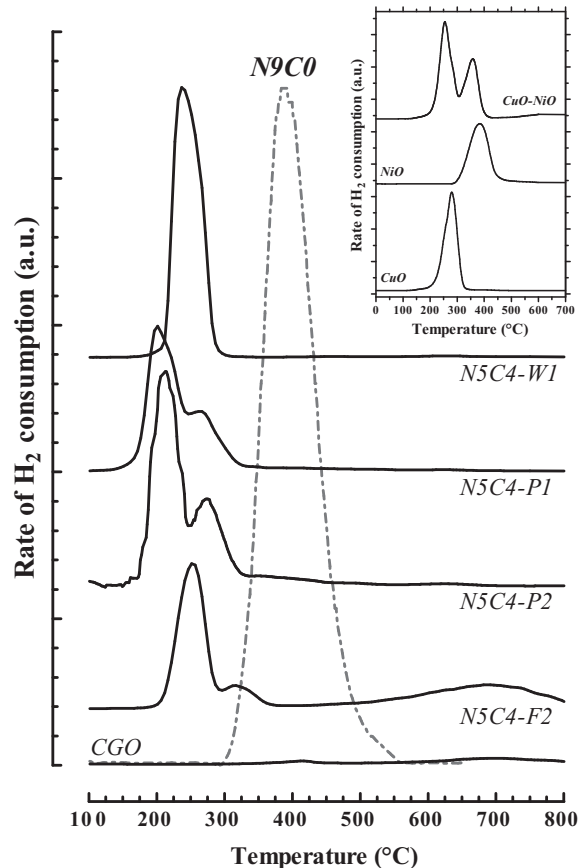


Fig. 3. Influence of the preparation method on the reduction profiles. In the inset, TPR profile of the reference “pure” metal oxides.

**Table 3**  
TPR data.

Catalyst	Reduction temperature (°C)			H <sub>2</sub> consumption		
	T <sub>0,red</sub>	T <sub>M0</sub>	T <sub>M1</sub>	T <sub>M2</sub>	mmol H <sub>2</sub> g <sub>cat</sub> <sup>-1</sup>	H <sub>2</sub> /(Cu + Ni) <sub>atm</sub>
CuO	192	280	–	–	–	1.00
NiO	277	–	383	–	–	1.00
CuO–NiO	175	255	350	–	9.6	0.74
N9CO	283	–	379	–	11.3	0.97
N5C4-W1	214	234	–	–	10.4	0.85
N5C4-P1	188	200	262	–	9.3	0.79
N5C4-P2	192	212	266	–	8.6	0.78
N5C4-F2	212	252	316	689	6.1	0.57
CGO	331	–	–	702	1.1	–

featuring the reduction of copper and nickel oxides respectively. As above discussed, although there are not sharp signals related to the diffraction peaks of NiO in XRD patterns of the N5C4-P1 and N5C4-P2 catalysts (Fig. 1), aggregated NiO patches may be present as small particles or in an amorphous phase that could be then reduced into metallic nickel along with reduction of CuO particles. However, a larger overlapping of the two reduction peaks of the N5C4-P1 sample accounts for the occurrence of a more intimate contact between Cu and Ni oxide particles, mirroring a metal dispersion slightly lower than that on the N5C4-P2 sample. On the other hand, the reduction maxima (T<sub>M0</sub> and T<sub>M1</sub>) of N5C4-P2 appear more resolved and shifted towards higher temperature (212–266 °C), likely due to the mechanical mixing procedure that causes a decrease in particle size (as discussed above), so favouring a stronger metal–support interaction and thus a higher reduction temperature [40]. Nevertheless, the TPR profile of the N5C4-F2 sample prepared by combustion of metal precursors and then mixing with CGO also shows two main reduction peaks below 350 °C. Namely, the reduction maxima of both NiO and CuO are shifted at higher temperature (252 and 316 °C), as a consequence of metal sintering occurring during the combustion step that, not only causes a lowering of surface area, but also results in a different distribution of particle sizes that affects the extent of interaction with the support upon mixing. Moreover, a minor H<sub>2</sub> uptake is also observable at high temperature (>500 °C), which could be ascribable either to the reduction of NiO<sub>i</sub> species [5,13,41], more strongly interacting with CGO compared to the other catalysts, or to the reduction of carbonate-like species [41] following the combustion step. The reduction profile of the catalyst prepared by impregnation (N5C4-W1) appears significantly different from the other investigated systems. Only one single reduction peak at 234 °C was detected, thus clearly indicating that the impregnation method, followed by calcination, favours the formation of uniform metal oxides particles easily reducible.

The occurrence of an interaction among the reducible species was further demonstrated by the reduction pattern of the CuO–NiO physical mixture, still characterized by two peaks related to CuO and NiO reduction, with maxima shifted of 25 and 33 °C lower than those of pure oxides. Instead, the reduction kinetics of the copper-free N9CO sample maintains almost unchanged the reduction maximum of NiO, 379 °C.

In quantitative terms, from data reported in Table 3, all the investigated catalysts exhibit a fairly high hydrogen consumption. In fact, starting from the uppermost value of the monometallic N9CO sample (11.3 mmol H<sub>2</sub>/g<sub>cat</sub>), corresponding to an almost stoichiometric reduction of NiO (0.97), the H<sub>2</sub> consumption for the NiCu/CGO systems ranges from 6.1 (N5C4-F2) to 10.4 mmol H<sub>2</sub>/g<sub>cat</sub> (N5C4-W1), accounting for a reduction stoichiometry (H<sub>2</sub>/Cu<sub>atm</sub> + Ni<sub>atm</sub>) of 0.57 and 0.85 respectively.

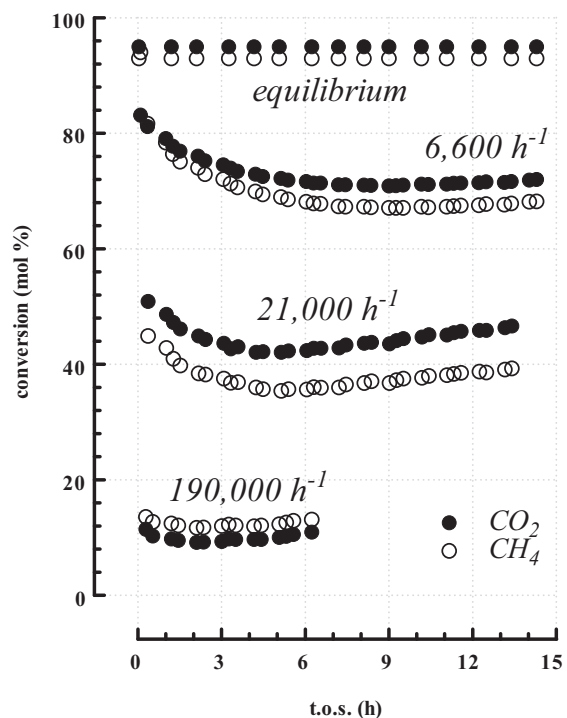
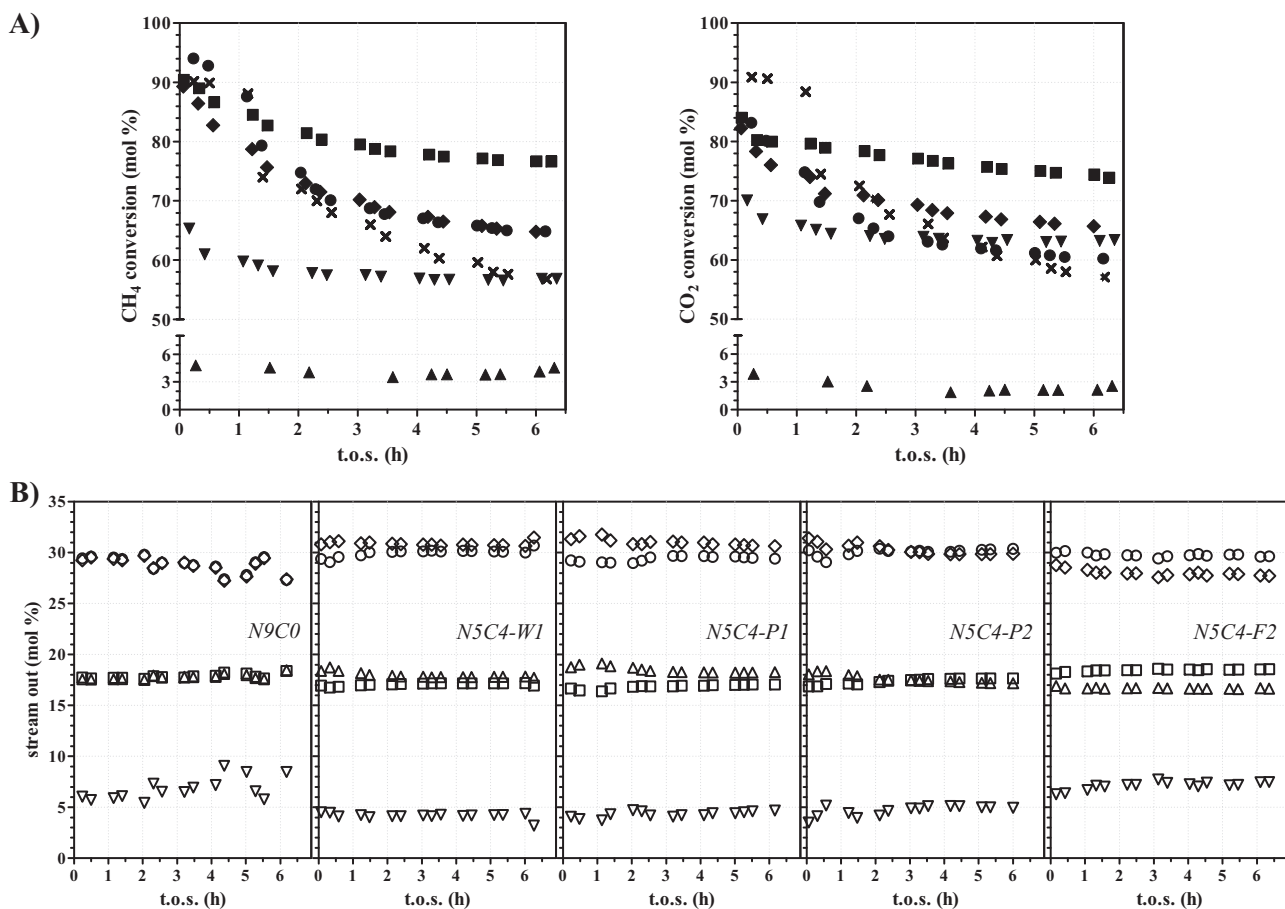


Fig. 4. Influence of space velocity on CH<sub>4</sub> and CO<sub>2</sub> conversion: T<sub>R</sub> = 800 °C; CO<sub>2</sub>/CH<sub>4</sub> = 1.

On the whole, TPR profiles clearly suggest that copper addition enhances the kinetics of nickel reduction. Indeed, the initial copper reduction would favour the hydrogen spillover, enhancing the rate of reduction of NiO species [42]. This phenomenon seems prevalent on the N5C4-W1 sample exhibiting, among the bimetallic catalysts, the highest reducibility value.

### 3.2. Catalytic testing

Taking into account that in dry reforming conditions, the deposition of carbon at 1 atm is thermodynamically possible with CO<sub>2</sub>/CH<sub>4</sub> mixtures in a 1:1 ratio up to 870 °C [27,43], preliminary tests were performed at 800 °C, at a temperature high enough to minimize the coke formation. These tests were carried out using the N5C4-P1 sample with a simulated biogas mixture (molar feed ratio CO<sub>2</sub>/CH<sub>4</sub> = 1), in a wide range of gas hourly space velocity (GHSV), between 6600 and 190,000 h<sup>-1</sup>. As expected, the higher the GHSV, the lower the conversion rates. In fact, from results shown in Fig. 4, it is easily observable that, at low space velocity (6600 h<sup>-1</sup>), conversions of CH<sub>4</sub> and CO<sub>2</sub> approach equilibrium values [43–45]. On the contrary, at high GHSV (190,000 h<sup>-1</sup>), CH<sub>4</sub> and CO<sub>2</sub> conversion values do not exceed 15%. Therefore, on the basis of these findings, the influence of reaction temperature (650–800 °C) on catalyst performance was evaluated at low GHSV (6600 h<sup>-1</sup>). In this condition, as reported in Table 4, the catalytic activity increases with reaction temperature, but catalyst deactivates with time on stream (t.o.s.): a difference between initial (10 min on stream) and final (6 h on stream) conversion values of both CO<sub>2</sub> and CH<sub>4</sub> at each temperature is observable. However, at 650 °C, catalyst shows the worst performance, with initial CO<sub>2</sub>–CH<sub>4</sub> conversion values of 47.5–43.9% which decrease until 17.7–15.0% after 6 h. A similar trend was observed at 700 °C, although a minor difference between initial CO<sub>2</sub>–CH<sub>4</sub> conversion (56.3–60.2%) and final conversion (32.0–26.0%) accounts for a slightly higher stability of the catalyst, still maintaining 43% of initial activity after 6 h. At last, at T<sub>R</sub> of 800 °C, catalyst exhibits the highest CO<sub>2</sub>–CH<sub>4</sub> conversion



**Fig. 5.** (A) Activity pattern ( $T_R = 800^\circ\text{C}$ ;  $\text{CO}_2/\text{CH}_4 = 1$ ;  $\text{GHSV} = 6600 \text{ h}^{-1}$ ) of the investigated catalysts (x, N9C0; ■, N5C4-W1; ●, N5C4-P1; ◆, N5C4-P2; ▼, N5C4-F2; ▲, CGO). (B) Product distribution at  $800^\circ\text{C}$  ( $\text{CO}_2/\text{CH}_4 = 1$ ;  $\text{GHSV} = 6600 \text{ h}^{-1}$ ) with t.o.s. (◊,  $\text{H}_2$ ; ○, CO; □,  $\text{CO}_2$ ; △,  $\text{CH}_4$ ; ▽,  $\text{H}_2\text{O}$ ).

values ranging from initial values of 83.2–94.0% to 60.2–64.8% after 6 h on stream; the lower deactivation rate was attributed to the minor formation of coke.

Once identified the suitable experimental conditions required to investigate the catalytic performance ( $T_R = 800^\circ\text{C}$ ;  $\text{GHSV} = 6600 \text{ h}^{-1}$ ), all catalysts were tested keeping the  $\text{CO}_2/\text{CH}_4$  feed ratio at 1. Under the same conditions, it has also been investigated the behaviour of “bare” CGO. In Fig. 5A and B, the activity pattern (in terms of  $\text{CH}_4$  and  $\text{CO}_2$  conversion) and the outlet stream composition are shown. CO,  $\text{H}_2$  and  $\text{H}_2\text{O}$  are the only products formed. As it is possible to see, from Fig. 5A, in the early hours of reaction a significant deactivation trend is observed for all the investigated systems, even if with a different extent. The reference copper-free N9C0 catalyst exhibits analogous initial (t.o.s. 30 min) values of  $\text{CO}_2$  and  $\text{CH}_4$  conversion (~90%), corresponding to the formation of  $\text{H}_2\text{O}$  (~6%) and equimolar amount of CO and  $\text{H}_2$  (~30%). On the other hand, the gadolinia-doped

cerium oxide (CGO) was characterized by a very low catalytic activity, with conversion values of  $\text{CO}_2$  and  $\text{CH}_4$  close to 3 and 4% respectively. This low activity is ascribable to the low reducibility of such material (see Fig. 3); in fact, as reported in literature, activity of cerium-based oxides depends on oxygen vacancy defects generated by surface reduction of ceria [46]. Moreover, the lowest CO concentration (~20%) detected in the outlet stream of CGO results in the highest  $\text{H}_2/\text{CO}$  ratio (1.67), much higher than the stoichiometric value (1.00) obtained on the reference N9C0 sample. With regard to the other systems, the catalysts prepared by impregnation (N5C4-W1) and coprecipitation (N5C4-P1 and N5C4-P2) show a similar behaviour, with comparable initial  $\text{CO}_2$  and  $\text{CH}_4$  conversion values (82–84% and 90–94% respectively), associated to similar concentration of  $\text{H}_2\text{O}$  (~4%),  $\text{H}_2$  (~31%) and CO (~29%) in the outlet stream. Indeed, the N5C4-W1 catalyst prepared by impregnation is also characterized by a good stability, since the activity loss after 6 h is less than 15%. Despite of similar initial conversion values, the coprecipitated N5C4-P1 and N5C4-P2 samples exhibit different deactivation kinetics. In fact, after 6 h of reaction, N5C4-P2 keeps levels of activity higher than N5C4-P1, attaining a total loss of  $\text{CH}_4$  and  $\text{CO}_2$  conversion of 27% and 20% respectively, against 31 and 28% of N5C4-P1. Besides, the initial catalytic activity of the N5C4-F2 catalyst prepared by combustion, either in terms of  $\text{CO}_2$  (70.1%) or  $\text{CH}_4$  conversion (65.3%), is lower in respect of the other catalysts. However, after a first step of steep deactivation, its conversion tends to level off over the time, remaining constant just after 2 h of reaction, either in terms of  $\text{CO}_2$  or  $\text{CH}_4$  conversion, with a net decrease of about 10% of the initial activity level. Yet, by comparing the results in terms of relative  $\text{CH}_4$  and  $\text{CO}_2$  conversion, only on the N5C4-F2 sample  $\text{CO}_2$  conversion is

**Table 4**

Activity of N5C4-P1 catalyst at different reaction temperature in  $\text{CO}_2$  reforming of  $\text{CH}_4$ .

$T_R$ (°C)	Initial conversion (%) <sup>a</sup>		Final conversion (%) <sup>b</sup>	
	$\text{CO}_2$	$\text{CH}_4$	$\text{CO}_2$	$\text{CH}_4$
650	47.5	43.9	17.7	15.0
700	56.3	60.2	32.0	26.0
800	83.2	94.0	60.2	64.8

$P_R = 1 \text{ atm}$ ;  $\text{GHSV} = 6600 \text{ h}^{-1}$ ;  $\text{CH}_4:\text{CO}_2 = 1:1$ .

<sup>a</sup> 10 min on stream.

<sup>b</sup> 6 h on stream.

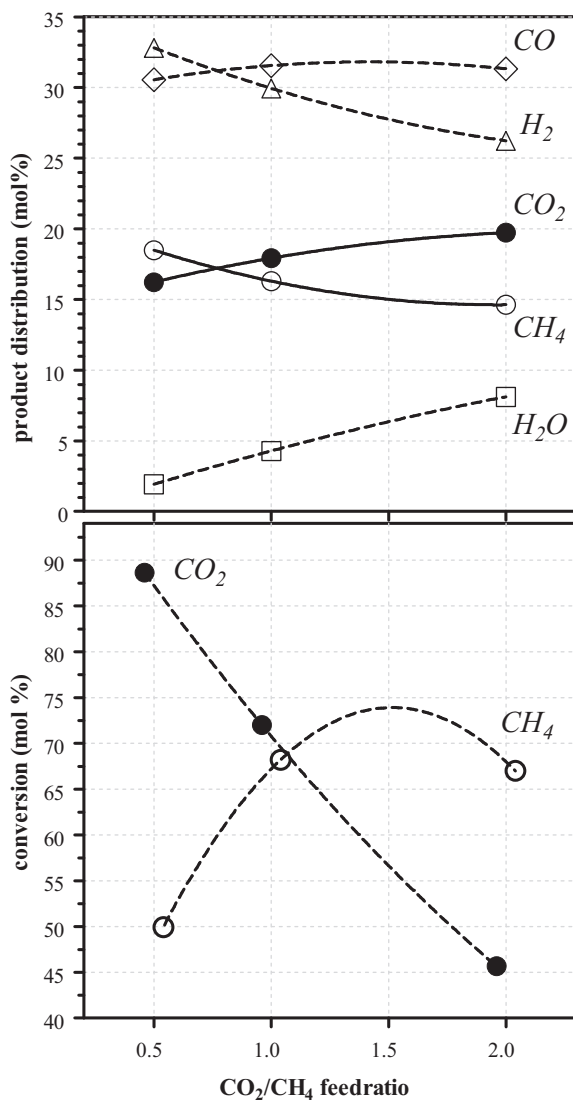


**Fig. 6.** Influence of the feed molar composition on the catalytic activity and product distribution of N5C4-P1 catalyst ( $T_R = 800^\circ\text{C}$ ; GHSV = 6600  $\text{h}^{-1}$ ; t.o.s. = 10 min).

higher than  $\text{CH}_4$  conversion for the whole reaction time, as well as the  $\text{H}_2/\text{CO}$  ratio (0.95) is lower compared to the other investigated catalysts (1.05–1.09). Over the copper-free N9CO sample, instead,  $\text{CH}_4$  and  $\text{CO}_2$  conversion values decrease in the same way, with an activity decay significantly higher than that observed on the other catalysts.

Considering the importance to identify the ideal feed composition to operate with high  $\text{H}_2$  productivity and low coking rate, some experiments were also carried out using the N5C4-P1 sample at a  $\text{CO}_2/\text{CH}_4$  ratio ranging from 0.5 to 2. The results obtained after 10 min on stream, in terms of reactants conversion and product distribution, are shown in Fig. 6. According to what reported by other authors [47] at  $\text{CO}_2/\text{CH}_4 = 0.5$  the conversion of  $\text{CH}_4$  results nearly 50%, while the conversion of  $\text{CO}_2$  reaches values close to 90%; under these conditions,  $\text{H}_2$  concentration in the products stream is slightly higher than that of  $\text{CO}$  (33 vs. 30%). On the contrary, by using a  $\text{CO}_2/\text{CH}_4$  ratio of 2, the conversion of  $\text{CO}_2$  drastically decreases (~45%), without being counterbalanced by an increase of  $\text{CH}_4$  conversion that, instead, maintains the same level reached at  $\text{CO}_2/\text{CH}_4 = 1$  (ca. 68%). Moreover, by feeding a  $\text{CO}_2$ -rich mixture, the concentration of  $\text{H}_2$  results to be lower than  $\text{CO}$  (26 vs. 31%), whereas the water concentration results to be

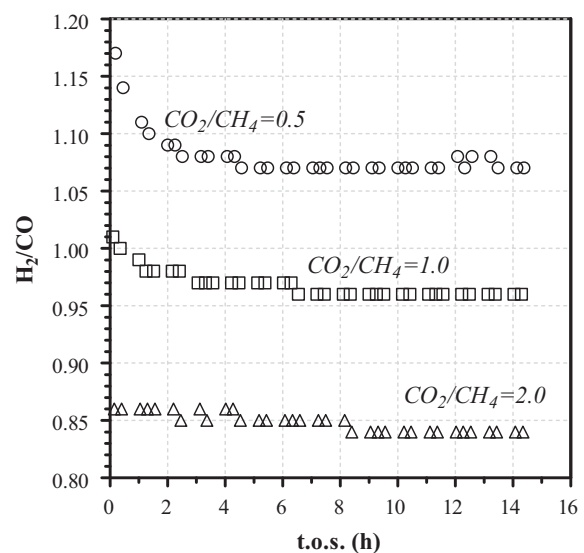


**Fig. 7.** Influence of the feed molar composition on the  $\text{H}_2/\text{CO}$  ratio of N5C4-P1 catalyst ( $T_R = 800^\circ\text{C}$ ; GHSV = 6600  $\text{h}^{-1}$ ).

increased from 1.92 to 8.11%. Such a product distribution results in a  $\text{H}_2/\text{CO}$  ratio (see Fig. 7) more than 1 in  $\text{CH}_4$ -rich mixtures (1.17 at  $\text{CO}_2/\text{CH}_4 = 0.5$ ), close to 1 under stoichiometric  $\text{CH}_4:\text{CO}_2$  concentration (1.01 at  $\text{CO}_2/\text{CH}_4 = 1$ ) and less than 1 in  $\text{CO}_2$ -rich mixtures (0.86 at  $\text{CO}_2/\text{CH}_4 = 2$ ). In any case, irrespective of stream composition, the  $\text{H}_2/\text{CO}$  ratio decreases with t.o.s. until reaching a plateau after ca. 15 h. However, by increasing the  $\text{CO}_2$  concentration in the feed, this decreasing trend appears more and more flat, as a consequence of a lower catalyst deactivation rate.

#### 4. Discussion

##### 4.1. Preparation method and physico-chemical properties of the catalysts

NiCu–CGO composite powders were synthesized by different preparation methods in order to find the most suitable way for producing fairly fine and homogenous metal oxide powders [48–51] to promote a good metal–support interaction which can enhance the resistance towards metal sintering along with the suppression of carbon formation even at low  $\text{CO}_2/\text{CH}_4$  feed ratio. Indeed, whereas segregation of the crystalline  $\text{CuO}$  (tenorite) and  $\text{NiO}$  (bunsenite) phase(s) (Fig. 1) matches the lower  $\text{SA}_{\text{BET}}$  of the N5C4-W1 and N5C4-F2 samples (Table 1), the improvement in textural properties (i.e. total area exposure and porosity) exhibited by N5C4-P1 and N5C4-P2 depends on the characteristics of the preparation method that allows precipitation of smaller oxide particles, ensuring a better mixing of the various precursors in the first stage of solid formation [52]. Moreover, an intimate contact among copper and nickel precursors can be also distinguished from the TPR profiles of the investigated catalysts (see Fig. 3). This could better account for the lower reduction temperature found for the bimetallic NiCu-containing samples, thus pointing out the promoter role of copper on nickel reducibility, at any extent of metal–support interaction.

Still, the metal content in cermets is another important variable having critical effects on the microstructure, sintering and anodic activities [53]. In general, a high metal loading provides a higher electrode conductivity, although it does not always ensure high anodic activities, because metal coalescence becomes more probable and the difference of thermal expansion between metal and carrier oxide component could seriously compromise SOFC lifetime. On this account, irrespective of the preparation method,

**Table 5**

List of reactions involved in the thermodynamic evaluation of the catalytic data.

Reaction	Stoichiometry	$\Delta H^\circ$ (kJ mol <sup>-1</sup> )	$K_p^a$
1	$\text{CH}_4 \rightleftharpoons \text{C} + 2\text{H}_2$	+75	2.20E+1
2	$\text{CO}_2 + \text{H}_2 \rightleftharpoons \text{CO} + \text{H}_2\text{O}$	+41	9.86E-1
3	$\text{C} + \text{H}_2\text{O} \rightleftharpoons \text{CO} + \text{H}_2$	+131	7.07E+0
4	$2\text{CO} \rightleftharpoons \text{CO}_2 + \text{C}$	-172	1.43E-1
5	$\text{CH}_4 + \text{H}_2\text{O} \rightleftharpoons \text{CO} + 3\text{H}_2$	+206	1.56E+2
6	$\text{CH}_4 + \text{CO}_2 \rightleftharpoons 2\text{CO} + 2\text{H}_2$	+247	1.53E+2

<sup>a</sup> Equilibrium pressure constant values at 800 °C with  $P_x$  values in bar.

NiCu alloys with a metal loading of about 60 wt% (see Table 1), although should involve a very low metal dispersion and then the existence of large particles on which the carbon growth should be favoured [54,55], anyway should enhance (electro)catalytic activity and resistance to carbon formation than monometallic copper-free Ni catalysts in dry reforming conditions [56–61].

#### 4.2. Thermodynamic analysis

$\text{CH}_4$  reforming with  $\text{CO}_2$  is a highly endothermic reaction favoured by low pressure and high temperature. A thermodynamic evaluation of the outlet stream composition [62] allows addressing the different reaction kinetics which depend on catalyst functionality and the thermodynamic factors thereon. In particular, as reported in Table 5, the dry reforming reaction can be described as a linear combination of a network involving the following reactions: (1) methane decomposition; (2) reverse water gas shift; (3) coal gasification; (4) Boudouard reaction; (5) steam reforming reaction. Therefore, both  $\text{CH}_4$  and CO are sources of carbon formation in  $\text{CO}_2$  reforming reaction. Then, substituting the experimental  $P_x$  values (from conversion-selectivity data) in the expression of the equilibrium constants, experimental  $K_{\text{exp}}$  values for the above reactions can be obtained. So, the ratio () between  $K_{\text{exp}}$  and the corresponding value of the equilibrium constant  $K_{\text{eq}}$  at 800 °C (Table 5) represents an index of the kinetics of the forward–reverse reactions, in terms of distance from equilibrium condition. In this respect, data shown in Fig. 8 point out that at 800 °C ( $\text{GHSV} = 6600 \text{ h}^{-1}$ ,  $\text{CO}_2/\text{CH}_4 = 1$ ) methane cracking, reverse water gas shift, coal gasification and methane steam reforming reactions take place, over all the investigated catalysts, under a full kinetic regime, being characterized by  $\beta_x$  values minor than 1 ( $\ln \beta_x < 0$ ). In particular, both on Ni and NiCu catalysts, the  $\beta_1$  values follow a similar trend, according to which the very low rate of methane decomposition reaction, far away from equilibrium constraints, represent the controlling step for the dry reforming reaction. Moreover, the trends of  $\beta_2$  and  $\beta_3$  indicate symmetrical reaction paths over all catalysts, suggesting a direct influence of the water formation on such reactions and accounting also for differences in the  $\text{H}_2/\text{CO}$  ratio. In particular, a  $\beta_2$  value higher than  $\beta_3$  should indicate a prevailing contribution of reverse water gas shift reaction in respect to carbon gasification. That is mainly relevant over the reference N9C0 and N5C4-F2 catalysts, on which a larger  $\text{H}_2\text{O}$  formation (7–9%) was detected in the outlet stream (see Fig. 5B) and, as a consequence, a lower  $\text{H}_2/\text{CO}$  ratio ( $\leq 1.0$ ) was obtained. Obviously, this finding is also in agreement with the catalytic results obtained over N5C4-F2, on which a prevailing availability of sites for  $\text{CO}_2$  activation has been inferred.

On the contrary, over N5C4-W1 and N5C4-P1, apart from slight initial differences, a  $\beta_3$  value just bigger than  $\beta_2$  mainly enhances the rate of carbon gasification, resulting also in a  $\text{H}_2/\text{CO}$  ratio larger than unity. As an intermediate behaviour among those above described, the N5C4-P2 sample, in agreement with the rate of  $\text{CH}_4$  and  $\text{CO}_2$  conversion (see Fig. 5A), exhibits a progressive decrease of  $\beta_3$  with t.o.s., paralleled by a steady increase of  $\beta_2$ , although such values result to be levelled off after 3 h on stream. On the other hand, either over Ni or NiCu systems,  $\beta_4$  is always larger than

that expected by thermodynamics ( $2.49 < \ln \beta_4 < 2.92$ ), mirroring a higher carbon dioxide concentration than that allowed by the highly exothermic and not favoured Boudouard reaction.

Indeed, at 800 °C,  $\text{CH}_4$  mainly reacts with  $\text{CO}_2$  to form CO. Hence, CO concentration largely determines the equilibrium carbon formation at high temperature in a  $\text{CO}_2$  reforming reaction. On the other hand, since water can be produced via reverse water gas shift reaction, methane steam reforming may compete with dry reforming, affecting so the  $\text{H}_2/\text{CO}$  ratio. However, due to a great distance from equilibrium, the contribution of methane steam reforming reaction ( $\beta_5$ ) results kinetically limited over all the investigated catalysts. Indeed, in the experimental conditions, water formation seems to represent the rate determining step for methane steam reforming reaction.

#### 4.3. Stability and deactivation of the catalysts

In order to shed light on the possible deactivation phenomena occurring with time over the catalysts, the  $\text{CH}_4$  conversion rate ( $X_{\text{CH}_4}$ ) was elaborated in terms of normalized activity, expressed as the ratio between  $\text{CH}_4$  conversion at time "t" ( $X_{\text{CH}_4,t}$ ) and initial  $\text{CH}_4$  conversion after 10 min on stream ( $X_{\text{CH}_4,0}$ ). Fitting with an exponential-decay function, a first-order deactivation rate was derived, according to which:

$$\ln \left( \frac{X_{\text{CH}_4,t}}{X_{\text{CH}_4,0}} \right) = -k_{\text{deact.}} t \quad (3)$$

So, consistently with the activity pattern of the investigated catalysts (see Fig. 5A), in Table 6 the deactivation constants ( $k_{\text{deact.}}$ ) are reported, resulting  $0.078 \text{ h}^{-1}$  for the copper-free N9C0 sample, which exhibits the highest loss of activity during t.o.s., and  $0.055 \text{ h}^{-1}$  for N5C4-F2 characterized by the highest stability.

With regard to the reasons that led to get a different trend of deactivation, certainly coking plays the main role. The stability and, hence, the activity of the catalysts corresponds to the ability of metals to decompose methane and dissociate  $\text{CO}_2$ : the  $\text{CO}_2$  dissociation produces adsorbed oxygen atoms that scavenge the carbon species formed. When the production rate of the carbon species on the surface is higher than the surface carbon oxidation rate, carbonaceous species would accumulate. To determine the amount of carbon deposited during the catalytic reaction ( $T_R = 800 \text{ °C}$ ;  $\text{GHSV} = 6600 \text{ h}^{-1}$ ;  $\text{CO}_2/\text{CH}_4 = 1$ ), thermogravimetric measurements of used samples were performed. As reported in Table 6, coke is formed both on monometallic and bimetallic surfaces, even if at a different extent. In particular, after 6 h on stream, less amounts of coke are formed on NiCu catalysts ( $5\text{--}45 \text{ mg}_C \text{ g}_{\text{cat}}^{-1}$ ) in respect of the coke deposited on Ni catalyst ( $\sim 75 \text{ mg}_C \text{ g}_{\text{cat}}^{-1}$ ). Although catalyst composition and preparation method, along with physical and chemical properties, are factors affecting the origin of carbon, such a lower coking capacity on NiCu alloys is likely due to a limited nickel activity towards  $\text{CH}_4$  decomposition and an enhanced carbon scavenge ability of  $\text{CO}_2$  induced by the addition of copper [63]. Accordingly to Alstrup et al. [64] the extent of NiCu alloy formation ( $\text{Cu}_{\text{at}}/\text{Ni}_{\text{at}} \geq 0.1$ ) inhibits carbon deposition, so explaining the superior stability of the CGO-supported NiCu alloy system in respect of the monometallic Ni-based catalyst. In addition, X-ray diffraction patterns of the used catalysts (herewith not shown) confirmed that graphitic carbon was present onto the catalyst surface of all samples. For this reason, in Fig. 9, the integrated peak area of carbon was plotted versus the coking capacity, so resulting in a straight-line relationship ( $r^2, 0.93$ ) confirming the reliability of the techniques (TG and XRD) used for the analytical determination of the carbonaceous deposits. However, a different intensity of the peak at  $2\theta = 26.5^\circ$  (JCPDS 26-1080) mirrors a different amount of the graphitic carbon deposited [65]. Moreover, after the reaction,

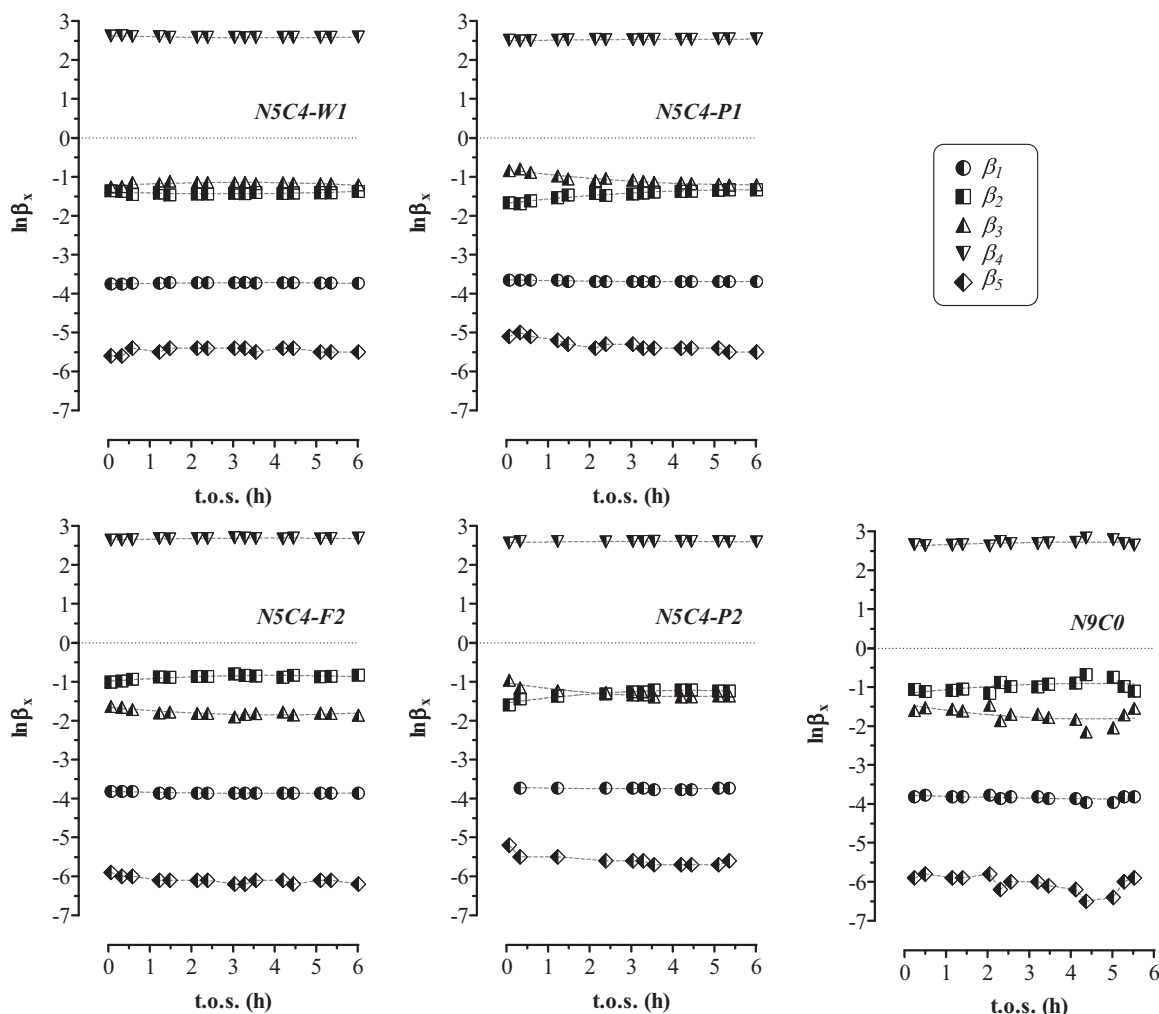


**Fig. 8.** CO<sub>2</sub> reforming of CH<sub>4</sub> ( $T_R$ , 800 °C; GHSV: 6600 h<sup>-1</sup>). Ratio ( $\beta$ ) between experimental and theoretical equilibrium constants of methane decomposition ( $\beta_1$ ), reverse water gas shift ( $\beta_2$ ), coal gasification ( $\beta_3$ ), Boudouard reaction ( $\beta_4$ ) and methane steam reforming reaction ( $\beta_5$ ) vs. t.o.s (h).

the cubic structure of NiCu alloy is always present, but changing in the phase composition was observed in comparison to the reduced samples. In this respect, the lattice spacing for the NiCu alloys of all systems ( $a_{220}$ , Table 6) is always larger than the values calculated on the reduced samples (Table 2), probably due to an expansion of the cell volume with time on stream. Such a lattice modification reflects a copper-enrichment of the alloy ( $\chi_{\text{Cu}}$ , Table 6), as also evidenced by the shift of the diffraction lines of the alloy towards lower angles. On the whole, these findings are in agreement with other authors [66], according to which nickel is selectively extracted from the bimetallic particles of the alloy to form large faceted crystals. As

a result, the alloy clusters are progressively surface-enriched into copper, then becoming more and more larger. At the same time, since the lattice parameter of the NiCu alloy, after the reaction, does not exceed that of “pure” copper (3.615 Å), the incorporation of carbon in the alloy crystallites can be excluded [67].

Besides, since from a quantitative point of view, the total amount of carbon accumulated over the various catalysts with t.o.s., except for the copper-free N9C0 sample, is quite small, it could be argued that catalyst deactivation of the investigated NiCu/CGO catalysts is not due only to coke deposition, but other surface processes should also be taken into account. Yet, again, from XRD data obtained by

**Table 6**  
Catalyst stability: deactivation constants, coking capacity, crystallographic parameters and average NiCu particle size ( $T_R$ , 800 °C; GHSV = 6600 h<sup>-1</sup>; CO<sub>2</sub>/CH<sub>4</sub> = 1).

Catalyst	$k_{\text{deact.}}^a$ (h <sup>-1</sup> )	Coking capacity <sup>b</sup> (mg <sub>C</sub> g <sub>cat</sub> <sup>-1</sup> )	$a_{220}^c$ (Å)	$\chi_{\text{Cu}}^d$	d <sub>s</sub> <sup>e</sup> (Å)	
					Reduced	Used
N9C0	0.078	73.4	–	0.000	152	315
N5C4-W1	0.061	14.1	3.567	0.482	222	277
N5C4-P1	0.071	46.0	3.568	0.483	161	281
N5C4-P2	0.069	38.5	3.566	0.468	192	288
N5C4-F2	0.055	5.6	3.569	0.490	258	284

<sup>a</sup> From analysis of normalized CH<sub>4</sub> conversion rate.

<sup>b</sup> Coke accumulation determined by TG analysis.

<sup>c</sup> Lattice spacing of NiCu alloy after use.

<sup>d</sup> Copper atomic fraction in the NiCu alloy after use.

<sup>e</sup> XRD values of reduced catalysts (before the reaction) and used catalysts (t.o.s., 6 h).

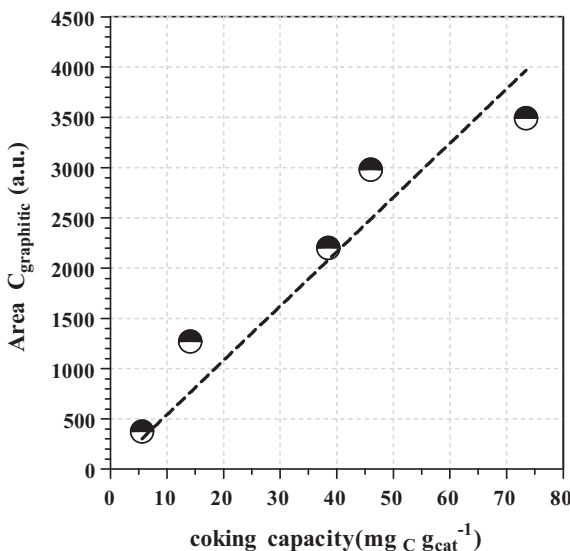


**Fig. 9.** Relationship between peak area of C (XRD analysis) and coking capacity (TG analysis) on the used samples ( $T_R = 800^\circ\text{C}$ ;  $\text{CO}_2/\text{CH}_4 = 1$ ;  $\text{GHSV} = 6600 \text{ h}^{-1}$ ; t.o.s.=6 h).

Sherrer's equation, the average NiCu particle size of "fresh" (i.e. reduced) and "used" catalysts was calculated, as diagnostic of the occurrence of potential metal sintering phenomena. As reported in Table 6, it is evident that, in the case of the copper-free N9C0 sample, a substantial reduction of Ni dispersion (i.e. increase of particle size) occurs under the adopted reaction conditions; in fact, the crystallite diameter changes from 152 to 315 Å. The increase of particle size, however, is significant for the N5C4-P1 (161 → 281 Å) and N5C4-P2 (192 → 288 Å) catalysts, whereas is small for the N5C4-W1 (222 → 277 Å) and N5C4-F2 (258 → 284 Å) catalysts. In any case a significant sintering of metal particles, under reaction conditions investigated, also accounts for the deactivation of catalyst.

In the attempt to rationalize the above experimental evidences, the deactivation constant values ( $k_{\text{deact.}}$ , Table 6), considered as dependent both on coking and sintering processes, were correlated with the coking capacity and with a factor related to the increasing of particle size, calculated as alteration of the NiCu alloy diameter after use in respect to the NiCu alloy diameter upon reduction (Fig. 10). As it is possible to observe, the deactivation constant linearly increases either with the accumulation of graphitic carbon on catalyst surface or with the sintering of metallic alloy particles, even

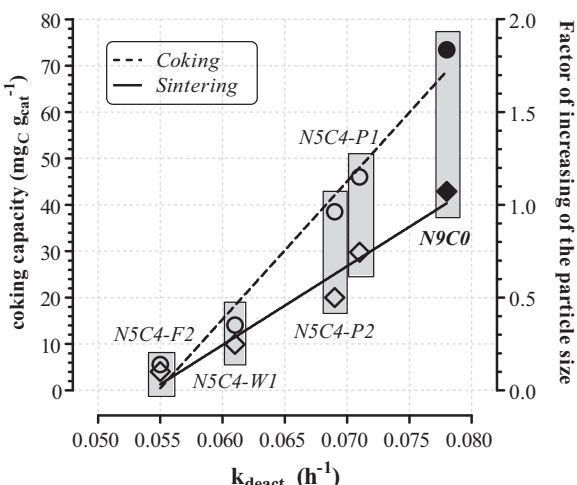


**Fig. 10.** Influence of (A) coking capacity and (B) metal particles sintering on the deactivation kinetics of N5C4-P1 catalyst at  $800^\circ\text{C}$  ( $\text{CO}_2/\text{CH}_4 = 1$ ,  $\text{GHSV} = 6600 \text{ h}^{-1}$ ).

if the different slopes of the two straight-line relationships highlight that kinetics of catalyst deactivation is fundamentally ruled out by coking ( $k_{\text{coking}}/k_{\text{sintering}} \approx 70$ ). In addition to carbon deposition and metal sintering, involvement of the catalyst carrier, via solid phase reactions with metallic sites, to form less active centers, or migration of species from the carrier onto the metallic surface, blocking active sites, may also contribute to catalyst deactivation [68]. In any case, the addition of Cu into the Ni catalyst system seems to stabilize the structure of the active sites, preventing the fast deactivation caused by coking and/or sintering phenomena.

#### 4.4. Influence of $T_R$ and $\text{CO}_2/\text{CH}_4$ feed ratio

Wang and Lu [69] concluded that methane decomposition is the main route for carbon deposition in  $\text{CO}_2$  reforming of  $\text{CH}_4$  but, at the same time, several others researchers [70,71] suggest that CO disproportionation is responsible for carbon formation. As previously discussed,  $\text{CH}_4$  decomposition is an endothermic reaction, so carbon formation is favoured at higher temperature; on the contrary, CO disproportionation is an exothermic reaction, thus, in this case, carbon formation will be favoured by decreasing the reaction temperature (below  $700^\circ\text{C}$ ) [72].

As reported in Fig. 11A, by operating with a  $\text{CO}_2/\text{CH}_4 = 1$  ratio, the amount of carbon formed over the N5C4-P1 sample increases as the temperature decreases; in particular, coking capacity was 57 and  $111 \text{ mg C gcat}^{-1}$  at  $700$  and  $650^\circ\text{C}$  respectively; in any case higher than that observed at  $800^\circ\text{C}$  ( $46 \text{ mg C gcat}^{-1}$ ). Therefore, irrespective of the preparation method, these findings confirm that coke accumulation significantly depends on reaction conditions. In particular, by decreasing the temperature until  $650^\circ\text{C}$ , the coke formation from Boudouard reaction becomes also possible and, as a consequence of a different oxygen availability, a different mechanism of carbon formation as a function of the reaction temperature is also expected. Indeed, a rise in the reaction temperature can increase the rate of all reaction pathways, such as rate of methane cracking, rate of  $\text{CO}_2$  dissociation and rate of surface carbon oxidation too. However, when the reaction temperature is close to  $800^\circ\text{C}$ , both  $\text{CO}_2$  dissociation and surface carbon gasification rate can be increased to a level that the carbon removal rate exceeds the carbon formation rate [43]. Then, the balance between carbon production and carbon removal rate gradually decreases with the decreasing of the reaction temperature and, thus, a higher catalyst stability at  $800^\circ\text{C}$  well accounts for the straight-line decrease of  $k_{\text{deact.}}$  with the reaction temperature (see Fig. 11A). On the other side, under the same reaction temperature, by using  $\text{CO}_2$ -lean mixtures (lower availability of oxygen species), the deposition of coke increases as shown in Fig. 11B. In fact, a coking capacity of  $128 \text{ mg C gcat}^{-1}$  was observed at  $800^\circ\text{C}$  with a  $\text{CO}_2/\text{CH}_4$  feed ratio of 0.5, instead, by operating with a  $\text{CO}_2/\text{CH}_4$  ratio of 2, the formation of coke is completely inhibited at  $800^\circ\text{C}$ , even if the  $\text{H}_2/\text{CO}$  ratio results to be decreased (see Fig. 7). Nevertheless, owing to the minor amount of carbon formation in presence of  $\text{CO}_2$ -rich biogas mixtures, the catalyst stability is also enhanced (see Fig. 11B), still stressing the prevailing role of coke deposition as primary cause of deactivating phenomena.

#### 4.5. TEM investigation

The nature of carbon formed over the bimetallic N5C4-P1 catalyst, as a function either of reaction temperature or  $\text{CO}_2/\text{CH}_4$  feeding ratio was investigated by TEM analysis. In Fig. 12, some TEM images of fresh N5C4-P1 sample, reduced at  $825^\circ\text{C}$ , are shown. CGO particles exhibit an irregular shape characterized by variable size comprised in the range 100–300 nm, whereas metal particles have a spherical morphology and they are regularly distributed on

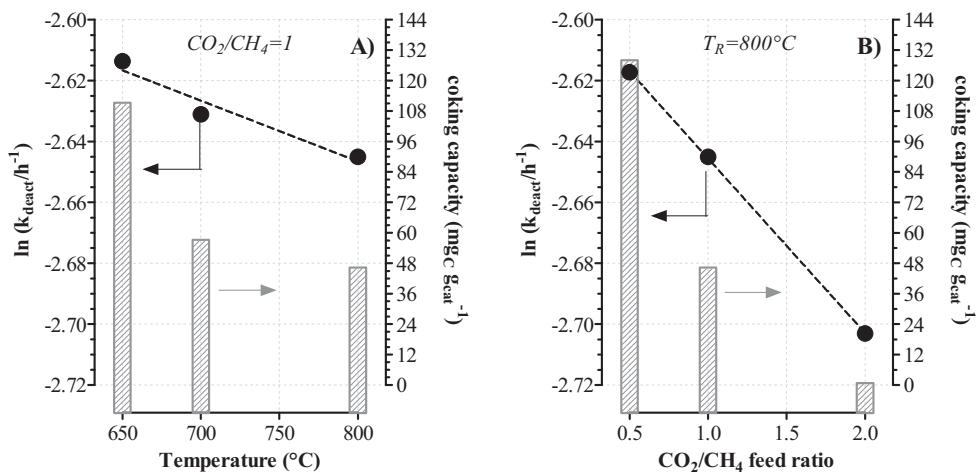


**Fig. 11.** Influence of reaction temperature (A) and CO<sub>2</sub>/CH<sub>4</sub> ratio (B) on carbon formation. Sample: N5C4-P1; t.o.s. = 360 min.

CGO surface. Specifically, metal particle size oscillates in the range 10–30 nm.

In agreement with literature evidences, it is well known that during reforming reaction catalyzed by Ni active phase, the type of carbon species formed, like amorphous carbon, crystalline graphite or filaments, depends on reaction conditions, but it is deeply affected also by metal particle size [25,65,73–76], metal ensemble [75,76] and metal–support interaction [25,75,76]. Such parameters control the diffusion rate of carbon into the metal particle. Specifically, when the rate of carbon diffusion through the metal catalyst particles is slower than that of the carbon formation at the surface metal sites, carbon builds up at the catalyst surface and eventually encapsulates the particle, hindering the nanofibers growth [64,77]. Therefore, carbon formed will be “encapsulating” or “filamentous”

with the particle at tip of filament. Basically, between the two types of carbon, the fibres formation has minor effect on the catalytic activity and the particles still maintain a clean active surface; on the contrary, when metal particles are encapsulated the deactivation rate is higher [77,78].

In Fig. 12, TEM images of “fresh” (A) and “used” catalysts (B–D) are shown. TEM image of fresh sample reveals that CGO particles have an irregular shape characterized by variable size comprised in the range 100–300 nm, whereas metal particles have a spherical morphology and they are regularly distributed on CGO surface. Specifically, metal particle size oscillates in the range 10–30 nm.

Images of sample used at 650 °C (A) and 700 °C (B) confirm the formation of carbon deposits, characterized by different morphology and structure: along with a diffuse and massive presence of

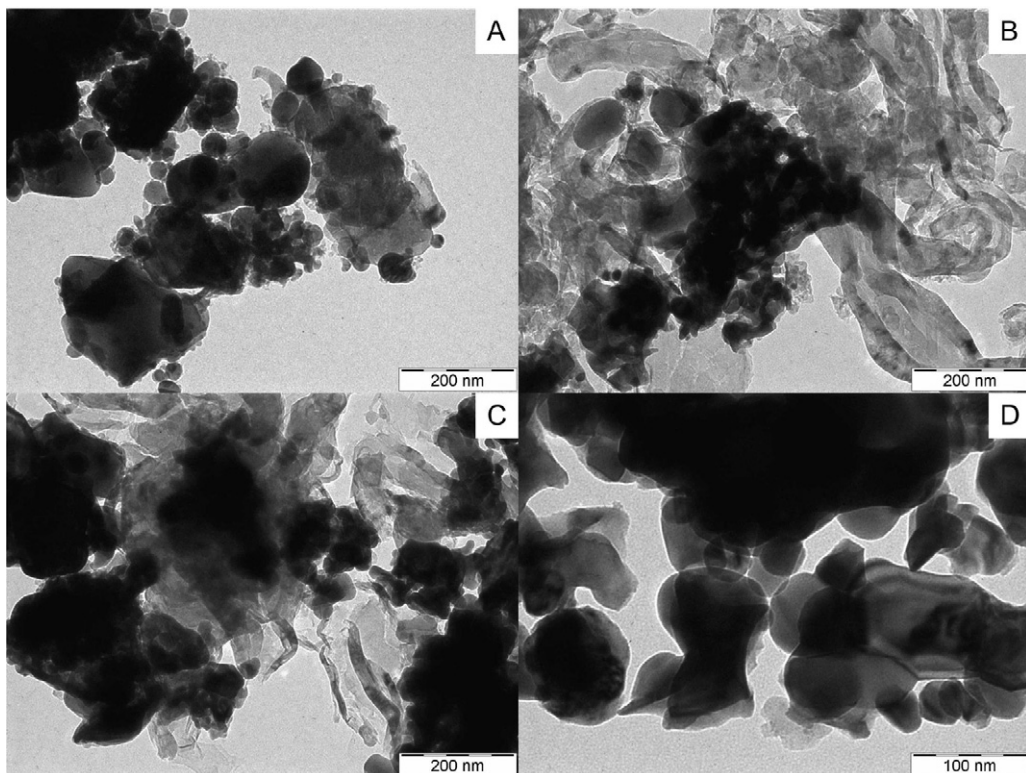


**Fig. 12.** TEM images of N5C4-P1 catalyst: (A) “fresh” catalyst, after H<sub>2</sub> reduction; (B–D) “used” catalyst at 650, 700 and 800 °C respectively (CO<sub>2</sub>/CH<sub>4</sub> = 1.0; GHSV = 6600 h<sup>-1</sup>; t.o.s. = 360 min).

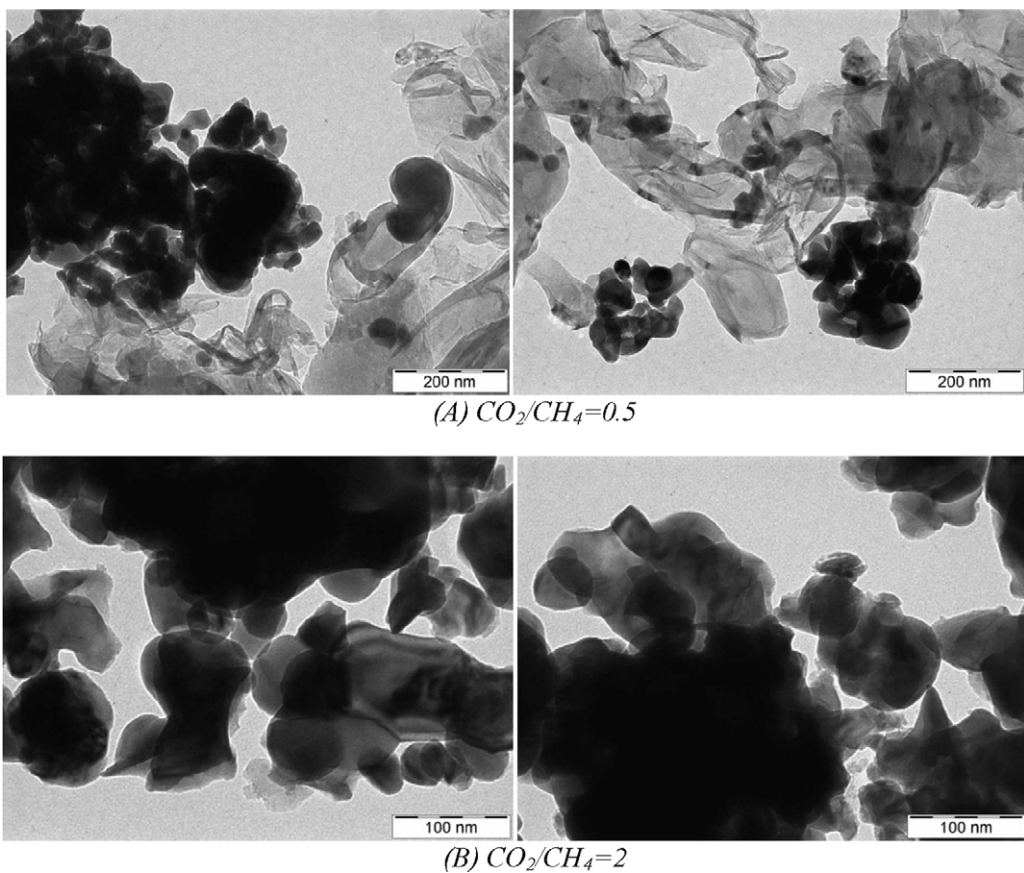


**Fig. 13.** TEM images of N5C4-P1 catalyst, “used” at 800 °C (GHSV = 6600 h<sup>-1</sup>; t.o.s. = 360 min): influence of  $\text{CO}_2/\text{CH}_4$  feed ratio on carbon formation.

large-sized amorphous and irregular carbon, filaments with metal at tip are evident too. Likewise, some metal particles are encapsulated by carbon deposits. From images B and C, it is possible to deduce that catalyst structure does not significantly change as reaction temperature increases from 650 to 700 °C. On the contrary, when reaction temperature increases to 800 °C (Fig. 12D) the catalyst structures changes. In fact, in this case, carbon is not extensively present on the catalyst surface and, moreover, morphology both of metal and support undergoes some modification. In particular, CGO attains a more spherical shape without significant variation in size, whereas the metal particles tend to achieve a medium size of about 30 nm. These evidences suggest that smaller particles present on fresh catalyst are more prone to sintering; anyway sintering phenomenon is very limited since particles size does not exceed 30 nm. Furthermore, in agreement with XRD measurements, this result could justify the drop in conversion values occurring during the first hours of reaction and then the following stabilization when particles attain their maximum value in size.

Therefore, from a global evaluation of such results, it is evident that reaction temperature plays a fundamental role in determining the extent and type of carbon formed during reaction. However, it is important to consider that, potentially, from a thermodynamic point of view, in dry-reforming conditions carbon could be formed even at 800 °C. Consequently, it seems reasonable to suppose that copper addition, besides limiting catalytic activity of Ni in the C–H bond cleavage reaction, preferentially eliminates large ensemble of Ni metal atoms, responsible for generation of carbon filaments, by “decoration” of the Ni metal surface [64,66,67].

As regards the  $\text{CO}_2/\text{CH}_4$  ratio effect on carbon formation, TEM images shown in Fig. 13 further confirm that, by feeding

$\text{CO}_2$ -lean biogas mixtures, carbon considerably forms also at 800 °C, so stressing that superficial oxygen concentration, derived from  $\text{CO}_2$  decomposition on metallic site, is a crucial factor to promote removal process of carbon coming from decomposition of both  $\text{CO}_2$  and  $\text{CH}_4$ .

## 5. Conclusions

$\text{NiCuO}_x$ –CGO composite powders ( $\text{NiCu:CGO} = 7:3$ ) suitable as anodic materials for SOFC devices were successfully prepared by various single or multi-step procedures and their activity and stability in the biogas dry reforming process were examined. All catalysts are active in the “dry reforming” reaction at atmospheric pressure, with a reaction temperature ranging from 650 to 800 °C at low space velocity (6600 h<sup>-1</sup>). By thermodynamic evaluation it was confirmed that the methane decomposition represents the rate limiting step of  $\text{CO}_2$  reforming reaction. However, both coking capacity and metal sintering were indicated as responsible for deactivation kinetics, although the prevailing role was ascribed to carbon deposition. In this respect, although the deactivation rate results higher at low temperature and in presence of  $\text{CH}_4$ -rich biogas mixtures, at low  $\text{CO}_2/\text{CH}_4$  feed ratio the  $\text{H}_2/\text{CO}$  ratio appears greater than 1, due to a minor contribution of the RWGS path. Irrespective of the preparation method and metal–support interaction,  $\text{NiCu}$  alloy always forms over all catalysts under  $\text{H}_2$  activation. On the whole, the addition of copper to Ni/CGO system appears to stabilize the active surface essentially by limiting the rate of coking along with metal particle sintering.

## Acknowledgement

Financial support by Ministero Sviluppo Economico (ROMA), in the frame of CNR-MSE agreement, is gratefully acknowledged.

## References

- [1] P. Leone, A. Lanzini, M. Santarelli, M. Calì, F. Sagnelli, A. Boulanger, A. Scaletta, P. Zitella, *Journal of Power Sources* 195 (2010) 239–248.
- [2] J. Van herle, F. Maréchal, S. Leuenberger, Y. Membréz, O. Bucheli, D. Favrat, *Journal of Power Sources* 131 (2004) 127–141.
- [3] R. Layi Fagbenle, A.B.C. Oguaka, O.T. Olakoyejo, *Applied Thermal Engineering* 27 (2007) 2220–2225.
- [4] M. Jenne, T. Dörk, A. Schuler, in: U. Bossel (Ed.), *Proceedings of the Fifth European Solid Oxide Fuel Cell Forum*, July 2002, Lucerne, Switzerland, 2002, pp. 460–466.
- [5] A. Kambolis, H. Matralis, A. Trovarelli, Ch. Papadopoulou, *Applied Catalysis A* 377 (2010) 16–26.
- [6] G. Valderrama, A. Kiennemann, M.R. Goldwasser, *Journal of Power Sources* 195 (2010) 1765–1771.
- [7] J. Guo, H. Lou, H. Zhao, D. Chai, X. Zheng, *Applied Catalysis A* 273 (2004) 75–82.
- [8] C.E. Daza, C.R. Cabrera, S. Moreno, R. Molina, *Applied Catalysis A* 378 (2010) 125–133.
- [9] A. Djaidja, S. Libs, A. Kiennemann, A. Barama, *Catalysis Today* 113 (2006) 194–200.
- [10] X.-Y. Quek, D. Liu, W.N.E. Cheo, H. Wang, Y. Chen, Y. Yang, *Applied Catalysis B* 95 (2010) 374–382.
- [11] M.V. Siviah, S. Petit, J. Barrault, C. Batiot-Dupeyrat, S. Valange, *Catalysis Today* 157 (2010) 397–403.
- [12] M.M. Barroso-Quiroga, A.E. Castro-Luna, *International Journal of Hydrogen Energy* 35 (2010) 6052–6056.
- [13] V.M. Gonzalez-DelaCruz, J.P. Holgado, R. Pereñiguez, A. Caballero, *Journal of Catalysis* 257 (2008) 307–314.
- [14] V. Sadykov, V. Muzykantov, A. Bobin, N. Mezentseva, G. Alikina, N. Sazonova, E. Sadovskaya, L. Gubanova, A. Lukashevich, C. Mirodatos, *Catalysis Today* 157 (2010) 55–60.
- [15] K. Nagaoka, K. Seshan, K.-I. Aika, *Catalysis Letters* 99 (2005) 97–100.
- [16] M. Garcia-Diéguez, I.S. Pieta, M.C. Herrera, M.A. Larrubia, L.J. Alemany, *Journal of Catalysis* 270 (2010) 136–145.
- [17] M. García-Diéguez, E. Finocchio, M.A. Larrubia, L.J. Alemany, G. Busca, *Journal of Catalysis* 274 (2010) 11–20.
- [18] K. Nagaoka, M. Okamura, K. Aika, *Catalysis Communications* 2 (2001) 255–260.
- [19] Z. Hou, P. Chen, H. Fang, X. Zheng, T. Yashima, *International Journal of Hydrogen Energy* 31 (2006) 555–561.
- [20] B. Nematollahi, M. Rezaei, M. Khajenoori, *International Journal of Hydrogen Energy* 36 (2011) 2969–2978.
- [21] A.I. Tsyganok, M. Inaba, T. Tsunoda, K. Suzuki, K. Takehira, T. Hayakawa, *Applied Catalysis A* 275 (2004) 149–155.
- [22] J. Mermelstein, M. Millan, N.P. Brandon, *Journal of Power Sources* 196 (2011) 5027–5034.
- [23] Z. Xie, C. Xia, M. Zhang, W. Zhu, H. Wang, *Journal of Power Sources* 161 (2006) 1056–1061.
- [24] J.-H. Lee, E.-G. Lee, O.-S. Joo, K.-D. Jung, *Applied Catalysis A* 269 (2004) 1–6.
- [25] S. Tang, L. Ji, J. Lin, H.C. Zeng, K.L. Tan, K. Li, *Journal of Catalysis* 194 (2000) 424–430.
- [26] Y.H. Hu, E. Ruckenstein, *Catalysis Reviews* 44 (3) (2002) 423–453.
- [27] J. Ogonowski, E. Skrzynska, *Catalysis Letters* 124 (2008) 52–58.
- [28] A. Sin, E. Kopnin, Y. Dubitsky, A. Zaopo, A.S. Aricò, D. La Rosa, L.R. Gullo, V. Antonucci, *Journal of Power Sources* 164 (2007) 300–305.
- [29] EG&Services Parsons, Inc, Science Applications International Corporation, Fuel Cell Handbook, 5 ed. (rev.), U.S. Department of Commerce, Springfield, VA, 2000, p. 138.
- [30] A.C. Furtado, C. Gonçalves Alonso, M. Pereira Cantão, N.R. Camargo Fernandes-Machado, *International Journal of Hydrogen Energy* 34 (2009) 7189–7196.
- [31] F. Wang, Y. Li, W. Cai, E. Zhan, X. Mu, W. Shen, *Catalysis Today* 146 (2009) 31–36.
- [32] J.S. Campbell, P.H. Emmett, *Journal of Catalysis* 7 (1967) 252–262.
- [33] S. Imamura, T. Yamashita, R. Hamada, Y. Saito, Y. Nakao, N. Tsuda, C. Kaito, *Journal of Molecular Catalysis A: Chemical* 129 (1998) 249–256.
- [34] F. Liu, S. Xu, L. Cao, Y. Chi, T. Zhang, D. Xue, *Journal of Physical Chemistry C* 111 (2007) 7396–7402.
- [35] H. Kim, C. Lu, W.L. Worrell, J.M. Vohs, R.J. Gorte, *Journal of the Electrochemical Society* 149 (2002) A247–A250.
- [36] L. De Rogatis, T. Montini, A. Cognigni, L. Olivi, P. Fornasiero, *Catalysis Today* 145 (2009) 176–185.
- [37] V. Ponec, *Applied Catalysis A: General* 222 (2001) 31–45.
- [38] F. Liu, C. Liu, X. Tao, S. Chen, *Journal of University of Science and Technology Beijing* 13 (4) (2006) 329–332.
- [39] J.A. Dean, *Lange's Handbook of Chemistry*, 15th ed., McGraw-Hill Inc., New York, 1999, pp. 4.31–4.32.
- [40] A. Parmaliana, F. Arena, F. Frusteri, N. Giordano, *Journal of the Chemical Society, Faraday Transactions* 86 (1990) 2663–2669.
- [41] H.-S. Roh, H.S. Potdar, K.-W. Jun, J.-W. Kim, Y.-S. Oh, *Applied Catalysis A* 276 (2004) 231–239.
- [42] J. Álvarez-Rodríguez, M. Cerro-Alarcón, A. Guerrero-Ruiz, I. Rodríguez-Ramos, A. Arcoya, *Applied Catalysis A* 348 (2008) 241–250.
- [43] S. Wang, G.Q. Max Lu, *Energy and Fuels* 10 (1996) 896–904.
- [44] K.-M. Kang, H.-W. Kim, Y.-W. Shim, H.-Y. Kwak, *Fuel Processing Technology* 92 (2011) 1236–1243.
- [45] A. Pietraszek, B. Koubaissy, A.C. Roger, A. Kiennemann, *Catalysis Today* 176 (2011) 267–271.
- [46] D.K. Kim, K. Stöwe, F. Müller, W.F. Maier, *Journal of Catalysis* 247 (2007) 101–111.
- [47] M. Wisniewsky, A. Boréave, P. Gélin, *Catalysis Communications* 6 (2005) 596–600.
- [48] J.J. Kingsley, L.R. Pederson, *Materials Letters* 18 (1993) 89–96.
- [49] D. Hari Prasad, H.-Y. Jung, H.-G. Jung, B.-K. Kim, H.-W. Lee, J.-H. Lee, *Materials Letters* 62 (2008) 587–590.
- [50] G. Bonura, F. Arena, G. Mezzatesta, C. Cannilla, L. Spadaro, F. Frusteri, *Catalysis Today* 171 (2011) 251–256.
- [51] D. Hari Prasad, H.-R. Kim, J.-W. Son, B.-K. Kim, H.-W. Lee, J.-H. Lee, *Catalysis Communications* 10 (2009) 1334–1338.
- [52] N.A. Dhas, A. Ektiarizadeh, K.S. Suslick, *Journal of the American Chemical Society* 123 (2001) 8310–8316.
- [53] D.W. Dees, T.D. Claar, T.E. Easler, D.C. Fee, F.C. Mrazek, *Journal of the Electrochemical Society* 134 (1987) 2141–2146.
- [54] J.R. Rostrup-Nielsen, *Journal of Catalysis* 85 (1984) 31–43.
- [55] J.R. Rostrup-Nielsen, *Studies in Surface Science and Catalysis* 68 (1991) 85–101.
- [56] E. Nikolla, J. Schwank, S. Linic, *Journal of Catalysis* 250 (2007) 85–93.
- [57] M.P. Humbert, C.A. Menning, J.G. Chen, *Journal of Catalysis* 271 (2010) 132–139.
- [58] C.M. Finnerty, N.J. Coe, R.H. Cunningham, R.M. Ormerod, *Catalysis Today* 46 (1998) 137–145.
- [59] D.L. Trimm, *Catalysis Today* 49 (1999) 3–10.
- [60] N.C. Triantafyllopoulos, S.G. Neophytides, *Journal of Catalysis* 217 (2003) 324–333.
- [61] G. Bonura, O. Di Blasi, L. Spadaro, F. Arena, F. Frusteri, *Catalysis Today* 116 (2006) 298–303.
- [62] F. Arena, G. Trunfio, E. Alongi, D. Branca, A. Parmaliana, *Applied Catalysis A* 266 (2004) 155–162.
- [63] H.-W. Chen, C.-Y. Wang, C.-H. Yu, L.-T. Tseng, P.H. Liao, *Catalysis Today* 97 (2004) 173–180.
- [64] I. Alstrup, M.T. Tavares, C.A. Bernando, O. Sørensen, J.R. Rostrup-Nielsen, *Materials and Corrosion* 49 (1998) 367–372.
- [65] J. Xu, Z. Wei, W. Jihui, L. Zhaojing, M.A. Jianxin, *Chinese Journal of Catalysis* 30 (11) (2009) 1076–1084.
- [66] M. Agnelli, C. Mirodatos, *Journal of Catalysis* 192 (2000) 204–214.
- [67] O.Y. Podyacheva, Z.R. Ismagilov, A.E. Shalagina, V.A. Ushakov, A.N. Shmakiv, S.V. Tsypulova, V.V. Kriventsov, A.V. Ischenko, *Carbon* 48 (2010) 2792–2801.
- [68] Z.L. Zhang, V.A. Tsipouriari, A.M. Efstatthiou, X.E. Verykios, *Journal of Catalysis* 158 (1996) 51–63.
- [69] S. Wang, G.Q. Lu, *Energy and Fuels* 12 (1998) 1235–1240.
- [70] M.C.J. Bradford, M.A. Vannice, *Applied Catalysis A* 142 (1996) 73–96.
- [71] J.Z. Zhang, X.E. Verykios, *Catalysis Today* 21 (1994) 589–595.
- [72] W. Pan, C. Song, *Catalysis Today* 148 (2009) 232–242.
- [73] J.J. Guo, H. Lou, X.M. Zheng, *Carbon* 45 (2007) 1314–1321.
- [74] J.G. Zhang, H. Wang, A.K. Dalai, *Journal of Catalysis* 249 (2007) 300–310.
- [75] F. Pompeo, N.N. Nichio, M.G. González, M. Montes, *Catalysis Today* 107–108 (2005) 856–862.
- [76] X. Chen, A.R. Tadd, J.W. Schwank, *Journal of Catalysis* 251 (2007) 374–387.
- [77] A. Carrero, J.A. Calles, A.J. Vizcaíno, *Applied Catalysis A* 327 (2007) 82–94.
- [78] H. Wang, R.T.K. Baker, *Journal of Physical Chemistry B* 108 (2004) 20273–20277.